Springer

KSME

Journal of Mechanical Science and Technology 24 (12) (2010) 2487~2495
www.springerlink.com/content/1738-494x
DOI 10.1007/s12206-010-0927-x

Numerical simulation of flows around axisymmetric inlet with bleed regions †

Einkeun Kwak, Hyungro Lee and Seungsoo Lee*

Department of Aerospace Engineering, Inha University, Incheon, 402-751, Korea

(Manuscript Received June 6, 2010; Revised August 22, 2010; Accepted August 31, 2010)

Abstract

A numerical simulation of flows in an axisymmetric supersonic inlet with bleed regions is performed. An existing code which solves the Reynolds Averaged Navier-Stokes equations and the two-equation turbulence model equations is converted into an axisymmetric code. In addition, a bleed boundary condition model has been applied to the code. In this paper, the modified code is validated by comparing numerical results against experimental data and other computational results for flows on a bump and over an oblique shock with bleed region. Using the code, numerical simulation is performed for the flows in an inlet with multiple bleed regions.

Keywords: Axisymmetric inlet; Bleed boundary condition; Numerical simulation; RANS equations; Two-equation turbulence models

1. Introduction

An inlet performs an important role in determining the performance of an air-breathing engine. The inlet system must be designed to maximize pressure recovery, lead stable airflow, provide correct and uniform mass flow, and minimize drag [1]. For a supersonic inlet, however, a fixed geometry suited to all conditions of engine operation does not exist. The interaction between shock waves and turbulent boundary layers can often result in inlet performance degradation as well as total failure of the inlet system. For a mixed compression supersonic inlet, "unstart" occurs when the inlet air flow supply and the engine-required flow have a mismatch. This results in shock waves that are violently expelled from the engine. This often leads to a compressor stall, a combustor blowout, and a large increase in drag, which, in turn, decrease the efficiency of the inlet system. Inlet buzz is a phenomenon of self-sustained shock oscillations that may appear in almost every type of supersonic inlets, and result in high-amplitude variations of the inlet mass flow and pressure. It generally occurs when the mass flow rate is reduced below a given value due to the ingestion of low momentum flow of the turbulent boundary layer, or the shear layer developed from the shock/boundary layer interactions and the shock/shock interactions. Inlet buzz can lead to thrust loss, engine surge, or even structural damages to the engine.

A porous bleed system alleviates the adverse effects of shock/boundary layer interactions by extracting a small fraction of the inlet core flow through perforations in the inlet surface that is upstream of the interactions. The bleed holes are usually located on the surfaces in bands or groups of rows. Bleed holes can be over a few hundred in number. The flow of low momentum is extracted through the bleed holes. Only the flow of higher momentum remains in the boundary layer, which withstands the adverse pressure gradient caused by the shocks. The secondary effect of the bleed system is to help stabilize the terminal shock near the inlet throat. As the terminal shock encounters the bleed regions in the throat, the increased level of bleed inhibits the upstream movement of the shock.

Traditionally, wind tunnels have been part of the primary research tools for supersonic inlet analysis and design. National Aeronautics and Space Administration (NASA) has performed experimental studies on the supersonic inlet system. Among them, Sorenson and Smeltzer [2] investigated an axisymmetric supersonic inlet known as NASA X-1507 inlet. However, due to the ever-increasing costs of wind tunnel testing, Computational Fluid Dynamics (CFD) has become a complementary or even an alternative research tool for the supersonic inlet performance analysis. Furthermore, recent developments in CFD methodologies and bleed modeling techniques allow for performing an analysis on the supersonic inlet with the bleed system. Abrahamson [3] conducted a numerical investigation on an axisymmetric inlet with bleed zones. In the study, Abrahamson used the Reynolds Averaged Navier-Stokes (RANS) equations with the Baldwin and Lomax turbulence model and the bleed model of Abrahamson and Brower [4]. Mayer and Paynter [5] developed a bleed model for the computation of supersonic inlet flows. Their

† This paper was recommended for publication in revised form by Associate Editor Do Hyung Lee

* Corresponding author. Tel.: +82 32 860 7358, Fax.: +82 32 865 5401
E-mail address: slee@inha.ac.kr

bleed boundary condition treats each bleed region as a porous wall. The flow velocity normal to the wall is computed based on local flow properties, total bleed area, and sonic mass flow coefficient. Sonic mass flow coefficient is the ratio of the actual flow rate to the ideal flow rate possible with isentropic flow assumption, which is correlated with the local Mach number and the pressure ratio of the plenum chamber and the total pressure. This boundary condition can be applied not only to steady state but to time-accurate calculations. Recently, Atkinson [6] performed numerical computations of an inlet using the 3-D Navier-Stokes equations with the Wilcox turbulence model. Instead of using a bleed model, he simply subtracted a specified mass flow rate from the solid wall. This simple model, however, does not account for the total pressure variation across the bleed wall.

One objective of this paper is to develop a performance prediction method for an inlet with the bleed system. The effects of the bleed and turbulence models on the computation, which have not been a topic of any research so far, are also examined. To achieve the goal, an existing 2-D RANS code [7] has been transformed to an axisymmetric code, and a bleed boundary condition model of Mayer and Paynter has been added to simulate flows over the NASA X-1507 inlet.

The paper is organized as follows. First, we present the governing equations for the mean flow and the turbulent quantities. Next, numerical methods to solve the governing equations will be briefly discussed. Mayer and Paynter's bleed boundary model is then discussed. Simulation results of the transonic flow around an axisymmetric bump and the supersonic flow over an oblique shock with bleed region will be presented to show the validity of the code. Inviscid simulation of the NASA X-2016 inlet and turbulent simulation of the NASA X-1507 axisymmetric inlet are presented and compared with experimental data. Finally, we end the paper with the concluding remarks.

2. Numerical methods

2.1 Governing equations

For the simulation of flows around supersonic axisymmetric inlets with bleed systems, the RANS equations and the two-equation turbulence model equations are chosen as governing equations. The equations can be cast as

$$\frac{\partial W}{\partial t}+\frac{\partial E}{\partial x}+\frac{\partial F}{\partial y}+\frac{G}{y}=\frac{\partial E_v}{\partial x}+\frac{\partial F_v}{\partial y}+\frac{G_v}{y}+S\,, \tag{1}$$

where W denotes the conservative variable vector; E and F are the inviscid flux vectors; E_v and F_v are the viscous flux vectors in each spatial directions. In this paper, x and y are the longitudinal direction and the polar direction of the cylindrical coordinates system, respectively. G and G_v are the flux vectors associated with the axisymmetry, and S is the source term vector of the turbulence model equations. The flux vectors are defined by

$$W=\begin{pmatrix}\rho\\ \rho u\\ \rho v\\ e\\ \rho s_1\\ \rho s_2\end{pmatrix},\ E=\begin{pmatrix}\rho u\\ \rho u^2+p\\ \rho uv\\ (e+p)u\\ \rho us_1\\ \rho us_2\end{pmatrix},\ F=\begin{pmatrix}\rho v\\ \rho vu\\ \rho v^2+p\\ (e+p)v\\ \rho vs_1\\ \rho vs_2\end{pmatrix},\ G=\begin{pmatrix}\rho v\\ \rho vu\\ \rho v^2\\ (e+p)v\\ \rho vs_1\\ \rho vs_2\end{pmatrix},$$

$$E_v=\begin{pmatrix}0\\ \tau_{xx}\\ \tau_{yx}\\ \Omega_x\\ (\mu_m+\sigma_{s1}\mu_t)\dfrac{\partial s_1}{\partial x}\\ (\mu_m+\sigma_{s2}\mu_t)\dfrac{\partial s_2}{\partial x}\end{pmatrix},\ F_v=\begin{pmatrix}0\\ \tau_{xy}\\ \tau_{yy}\\ \Omega_y\\ (\mu_m+\sigma_{s1}\mu_t)\dfrac{\partial s_1}{\partial y}\\ (\mu_m+\sigma_{s2}\mu_t)\dfrac{\partial s_2}{\partial y}\end{pmatrix},\ G_v=\begin{pmatrix}0\\ \tau_{xy}\\ \tau_{yy}-\tau_{\theta\theta}\\ \Omega_y\\ (\mu_m+\sigma_{s1}\mu_t)\dfrac{\partial s_1}{\partial y}\\ (\mu_m+\sigma_{s2}\mu_t)\dfrac{\partial s_2}{\partial y}\end{pmatrix}, \tag{2}$$

where ρ, u, v, e, s_1, and s_2 are the density, axial velocity component, radial velocity component, specific total energy, and turbulent variables, respectively. Moreover, τ_{ij} and Ω_i are the total stress tensor, and the total energy flux vector, respectively. The equation of state for an ideal gas is used.

2.2 Numerical schemes

Upon applying a finite volume method to Eq. (1), the semi-discretized equation is found to be

$$\frac{dW}{dt}+R=0\,, \tag{3}$$

where the residual R is defined by

$$R=\frac{1}{V}\Big\{\big(\bar{F}\Delta S\big)_{i+1/2}-\big(\bar{F}\Delta S\big)_{i-1/2}+\big(\bar{F}\Delta S\big)_{j+1/2}-\big(\bar{F}\Delta S\big)_{j-1/2}\Big\}+\tilde{S}\,. \tag{4}$$

In Eq. (4), the total flux vector is defined as the sum of the inviscid flux vector and the viscous flux vector, while the total source term is defined by

$$\bar{F}=\bar{F}_c-\bar{F}_v\,,\ \tilde{S}=\frac{(G-G_v)}{y}-S\,. \tag{5}$$

Roe's approximated Riemann solver [8] and the central difference method are used for calculating inviscid flux vectors and viscous flux vectors, respectively. Van Leer's Monotone Upstream centered Schemes for Conservation Laws (MUSCL) extrapolation [9] with limiters is used to obtain the second order accuracy while maintaining the Total Variation Diminishing (TVD) property. In this paper, van Albada's limiter is used because it is continuously differentiable. To advance Eq. (3) in time, Approximate Factorization-Alternative Direction Implicit (AF-ADI) scheme [10] is used. Using Crank-Nickolson method, Eq. (3) can be re-written as

$$\frac{\Delta W}{\Delta t}+\theta R^{n+1}+(1-\theta)R^{n}=0\,. \tag{6}$$

The superscript n denotes time step. Eq. (6) can be linearized as follows:

$$\left[D+\frac{\theta\Delta t}{V}(A+B)\right]\Delta W=-\Delta tR\,. \tag{7}$$

Applying AF-ADI scheme, Eq. (7) becomes a block tri-diagonal matrix system and can be solved easily by

$$\left[D+\frac{\theta\Delta t}{V}A\right]D^{-1}\left[D+\frac{\theta\Delta t}{V}B\right]\Delta W=-\Delta tR\,. \tag{8}$$

Details of the numerical schemes can be found in [11].

2.3 Turbulence models

Two turbulence models are used to compute turbulent quantities. One is Coakley's $q-\omega$ model [12] and the other is Menter's $k-\omega$ SST model [13]. The models based on ω have the advantage of implementing a bleed boundary condition. Coakley's model uses the turbulent velocity scale and the specific dissipation rate to estimate eddy viscosity. Eddy viscosity is computed with the Prandtl-Kolmogorov relation

$$\mu_t=C_\mu D_q\frac{\rho q^2}{\omega}\,, \tag{9}$$

where C_μ =0.09. The damping function is defined by

$$D_q=1-\exp(-0.022R_q)\,,\ R_q=\frac{\rho qy}{\mu}\,, \tag{10}$$

where y is the normal distance from the nearest solid wall.

Menter's $k-\omega$ SST model is one of the most popular turbulence models in aerodynamics. The SST model is developed from $k-\omega$ BSL model to account for the shear stress transport of adverse pressure gradient boundary layers. The BSL model is a hybrid model which combines the $k-\omega$ model in the near wall region and the $k-\varepsilon$ model in the outer region. The eddy viscosity of the SST model is computed as follows

$$\nu_t=\frac{a_1k}{\max(a_1\omega;\Omega F_2)}\,, \tag{11}$$

$$\arg_2=\max\left(2\frac{\sqrt{k}}{0.09\omega y};\frac{500\nu}{y^2\omega}\right), \tag{12}$$

$$F_2=\tanh\left(\arg_2^2\right). \tag{13}$$

2.4 Bleed boundary condition

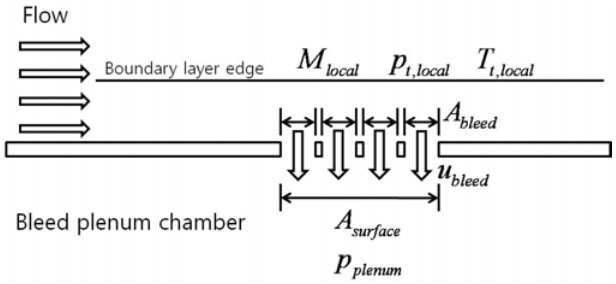

Fig. 1. Schematic of the constant-pressure bleed model($\alpha_{bleed}=90°$).

As stated in the introduction, many supersonic inlets use a bleed system to control boundary layer build-up and to increase shock stability. It is not practical to include the perforations in the simulation of the flow field induced by the bleed system. Instead, a constant pressure bleed model proposed by Mayer and Paynter is selected for simulation of the bleed regions.

The schematic of the bleed model is presented in Fig. 1. The bleed model regards the bleed region as a porous wall and computes the bleed velocity normal to the wall from the local flow properties, porosity, Φ , and sonic mass flow coefficient, Q_{sonic} . Porosity is defined by the ratio of the surface area of the bleed region ($A_{surface}$) to the total area of the bleed holes (A_{bleed}),

$$\Phi=\frac{A_{bleed}}{A_{surface}}\,. \tag{14}$$

Sonic mass flow coefficient is the ratio of the maximum mass flow in ideal condition to the actual bleed mass flow. It can be interpolated from the experimental data using the angle of holes, α_{bleed} , the local Mach number, M_{local} , and the ratio of the plenum chamber pressure, p_{plenum} to the local total pressure, $p_{t,local}$. The sonic mass flow coefficient is defined by

$$Q_{sonic}\equiv\frac{\dot m_{actual}}{\dot m_{ideal}}=f\left(\alpha_{bleed},M_{local},\frac{p_{plenum}}{p_{t,local}}\right). \tag{15}$$

The properties at the edge of the boundary layer are used as local properties. Bleed velocity is computed from the one-dimensional nozzle equation and the definition of the sonic mass flow coefficient

$$u_{bleed}=Q_{sonic}\Phi\frac{T_wp_{t,local}}{p_w\sqrt{T_{t,local}}}\sqrt{\gamma R}\left(\frac{\gamma+1}{2}\right)^{-\frac{\gamma+1}{2(\gamma-1)}}. \tag{16}$$

The subscript w denotes the properties in the wall. The bleed velocity computed from Eq. (16) is used to specify the normal velocity component through Eq. (17),

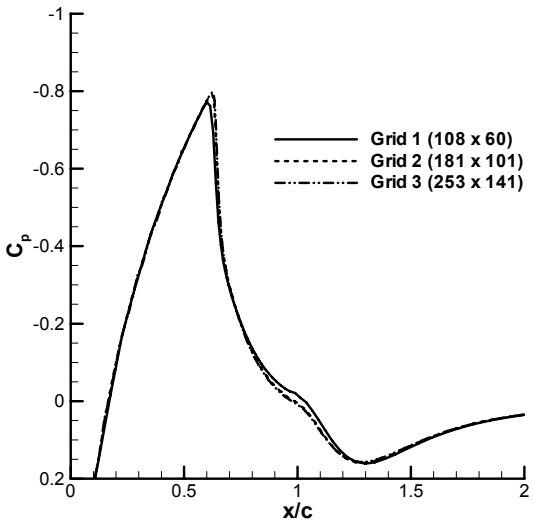

Fig. 2. The wall pressure distributions with three different grids.

$$\vec{u}_w = \vec{u}_w + u_{bleed}\hat{n}_w \,. \tag{17}$$

Modification of the boundary condition of the turbulent quantity, ω, is required for the wall boundary with roughness and mass injection, whereas the smooth wall boundary condition can be used for the wall boundary with suction or bleed [14]. In the present work, the roughness effect is the only one considered to achieve a specific inflow condition in the computation of flow over an oblique shock with bleed regions. Details of the wall boundary condition with roughness and mass injection can be found in the same reference.

3. Computational results

3.1 Turbulent flow around axisymmetric bump and over an oblique shock with bleed regions

For the validation of the code developed in this paper, the numerical simulation of a flow over an axisymmetric bump is performed. Results of the simulation are compared against the experimental data of Johnson et al. [15] and other computational results of Barakos and Drikakis [16]. The Mach number of the flow is 0.875 and the unit Reynolds number is 13.6×10^6 per meter. Grid convergence test is also performed on this problem with three different grids. The computed pressure coefficients are presented in Fig. 2. From this figure, no significant differences are revealed between Grids 2 and 3. Thus, Grid 2 is chosen for the simulations. The close-up view of the selected grid is shown in Fig. 3. The length of the bump (c) is 20.3 cm. The three lines in Fig. 3 denote locations where comparisons of the velocity profile are made. Lines (1), (2), and (3) are located at $x/c = 0.75$, 1.0, and 1.125, respectively.

The comparisons of velocity profile and turbulent kinetic energy profile are presented in Figs. 4 and 5. Computational results of this study agree well with other results. The results using the $k-\omega$ SST model are in excellent agreement with the experimental data in the separation region. In Barakos and

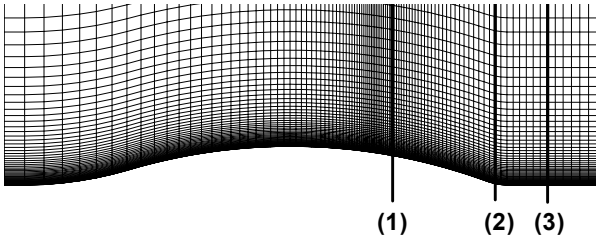

Fig. 3. The computational grid near the bump.

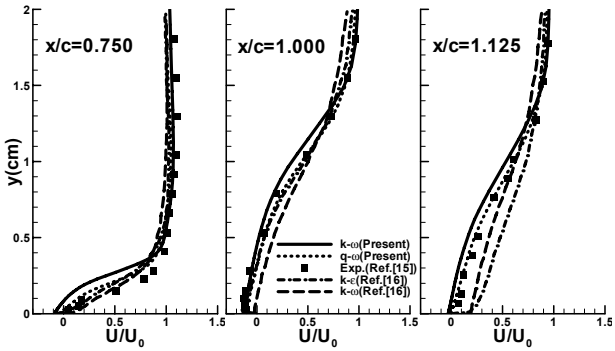

Fig. 4. Comparisons of the velocity profiles at axial locations.

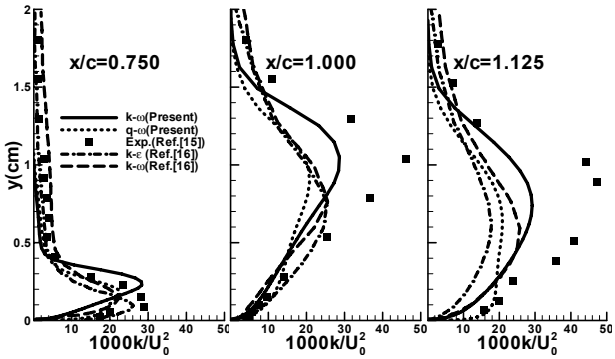

Fig. 5. Comparisons of turbulent kinetic energy at axial locations.

Drikakis's numerical computations, a characteristic flux extrapolation method [17] for the inviscid flux was used while the same $k-\omega$ SST model was used for the turbulence model, which gives the difference in the velocity profile and the turbulent kinetic energy from the present method, as can be seen in Figs. 4 and 5.

The bleed boundary condition implemented in the present code has been validated and presented elsewhere [18]. The results are summarized briefly. Willis et al. [19] conducted an experiment of a flow over an oblique shock between a flat plate with bleed region and a flat plate with an 8 degree slope.

Simulation results using the code are compared against the experimental data by Willis et al. Fig. 6 depicts a computational grid of 226×80 used for the computation. Boundary conditions specified for the simulation are also presented in the same figure. The Mach number of the flow is 2.46 and the unit Reynolds number is 1.81×10^7 per meter. The velocity profiles and incompressible shape factors at 18 cm down-

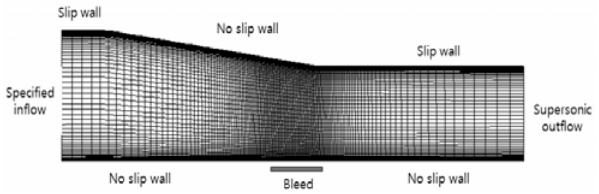

Fig. 6. Computational grid, and boundary conditions.

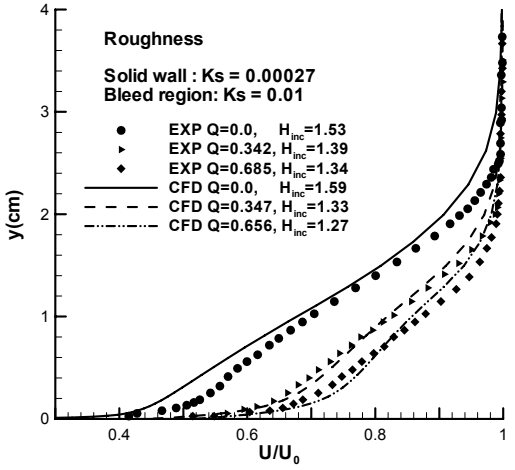

Fig. 7. Comparisons of normalized velocity profiles, Sonic mass flow coefficients and incompressible shape factors.

stream of the bleed starting point are shown in Fig. 7. The results are in good agreement with the experimental data.

3.2 Inviscid flow around 2-D supersonic inlet with back pressure boundary condition

For the simulation of flows around inlets, back pressure, or mass flow boundary conditions are widely used at an engine face or at an exit. In this study, the back pressure boundary condition is chosen. For a supersonic inlet, however, care must be taken when these boundary conditions are applied because they require the flow to be subsonic at the exit. For this reason, the simulation is conducted with a three-step method. The simulation starts from a supersonic initial condition and the supersonic exit boundary condition specified at the exit. After the main flow features in the supersonic region are developed, re-initialization of the solution from the throat to the engine face is performed. Using isentropic relations, the supersonic flow inside the inlet duct is decelerated so that the flow at the exit becomes subsonic. The simulation is restarted from the solution with a desired back pressure.

To validate the three-step method, a 2-D mixed compression inlet, which was used for the numerical study by Jain and Mittal [20], is selected. The inlet geometry was modified by Jain and Mittal from the original geometry used by Anderson and Wong [21] for their experimental investigations. The free-stream Mach number is 3 and the details of the experiment are available in [20, 21]. Fig. 8 shows the Mach number contour

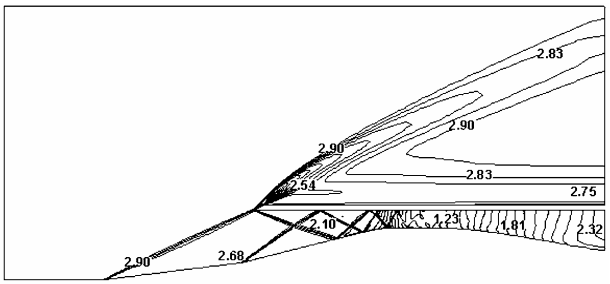

(a) Step 1: Simulation from supersonic initial condition with supersonic exit boundary condition

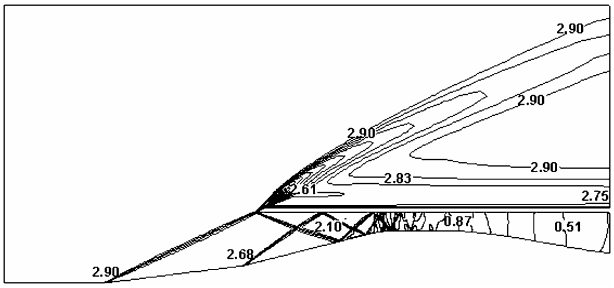

(b) Step 2: Re-initialization using the isentropic relation

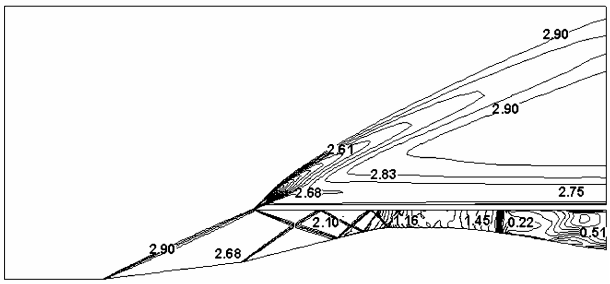

(c) Step 3: Simulation result with a proper back pressure boundary condition

Fig. 8. Procedure of the three-step simulation (Mach number contours).

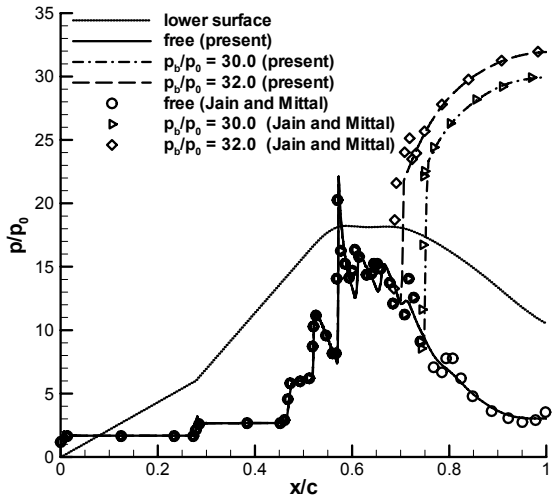

Fig. 9. Comparisons of the wall static pressure distributions at various back pressures.

plot obtained with the three-step procedure.

The wall static pressure distributions along a lower surface are shown in Fig. 9. Pressure distributions marked as "free" on the plot are the results of supersonic exit boundary condition while the others are the results with back pressure boundary conditions with p_b / p_0 = 30.0 and 32.0. The positions of shocks and the flow features in Fig. 9 are in good agreement with Jain and Mittal's numerical results. The three-step method is applied to all computations presented in the next section.

3.3 Turbulent flow around an axisymmeric supersonic inlet with bleed regions

The axisymmetric supersonic and mixed compression inlet, which was employed by Sorenson and Smeltzer [2] for their experimental investigations, is chosen for the simulation. There exist two bleed regions on both the cowl and the center-body. In their study, Sorenson and Smeltzer investigated the effects of the various bleed settings and vortex generators. Each bleed setting has different plenum chamber pressure to control the range of bleed mass-flow ratio. In this study, only two cases are chosen for numerical investigation. Case 1 indicates the case without vortex generators and with bleed setting A, while Case 2 indicates the case with vortex generator and with bleed setting B. The details of the bleed settings A and B are given in reference [2]. Slater and Saunders used Case 2 as a test-bed for their bleed boundary condition [22]. The vortex generator is ignored in case 2, as done in Slater and Saunders's study.

The free-stream is Mach 3 flow and the unit Reynolds number is 2.0×10^6 per foot. The computational grid consists of two blocks with grid sizes of 213×80, and 597×100, respectively. The locations of the four bleed regions and the grid near the throat are shown in Fig. 10. The bleed regions of ZONES I and II contribute to preventing the separation induced by the interaction between oblique shock and boundary layer. ZONES III and IV help in controlling the terminal shock near the throat. For all bleed regions, the bleed hole angle is 90° and the porosity is 41.5%. The diameters of the bleed holes are 0.025 (ZONE I) and 0.125 inch (ZONE II, III, IV). As stated earlier, a pressure of the bleed plenum chamber is required to apply the bleed boundary condition. In Sorenson and Smeltzer's paper, the plenum chamber pressure, however, was not given for Case 1. The plenum chamber pressure, therefore, is estimated from the plenum chamber pressure for the cases with the vortex generator through interpolations.

The flows of the inlet are categorized as supercritical, critical, and subcritical conditions according to the shock position as the engine face condition varies. The flow field of the computational domain is presented in Fig. 11. The Mach number contour plots near the terminal shock at three different states are shown in Fig. 12. In the supercritical condition, the terminal shock is located downstream of all bleed regions and the bleed mass flow is not changed by moving the terminal shock.

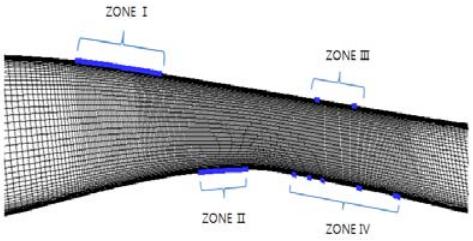

Fig. 10. The grid system near the throat and bleed regions.

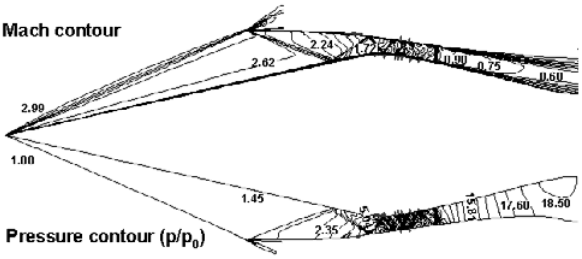

Fig. 11. Mach and pressure contour plots.

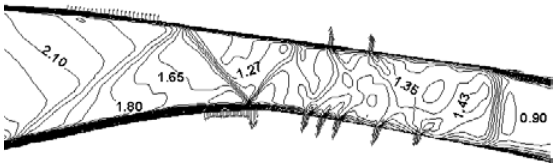

(a) Supercritical condition

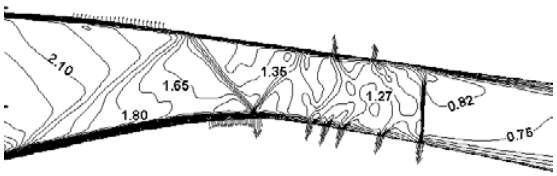

(b) Critical condition

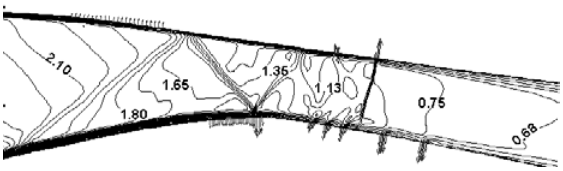

(c) Subcritical condition

Fig. 12. Three states of inlet condition near the terminal shock positions.

In the critical condition, the terminal shock is located at the end of the bleed regions and the inlet operates at an optimal condition. In the subcritical condition, the terminal shock violates the bleed regions and the loss of mass flow increases. If the terminal shock moves further upstream, the inlet will eventually "unstart."

3.3.1 Case 1

The simulation of the inlet without the vortex generators and with the bleed setting A is considered first. As mentioned earlier, the pressure in the bleed plenum chamber was not

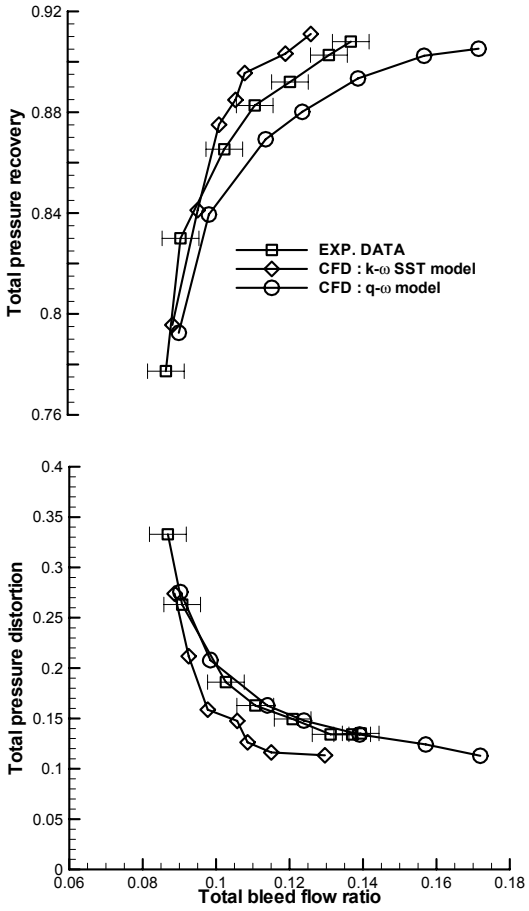

Fig. 13. Total pressure recoveries and total pressure distortions at various total bleed flow ratios.

given for this case. The plenum chamber pressure at the engine face, however, was given for the cases with the vortex generators. Therefore, the pressure data are estimated from the cases with the vortex generators by interpolations. The simulation is performed with the $q-\omega$ model and the $k-\omega$ SST model. These results are compared against the experimental data of Sorenson and Smeltzer. Fig. 13 shows the total pressure recovery ($\overline{p}_{t2}/p_{t0}$) and the total pressure distortion (Δp_{t2}) at the engine face as functions of the total bleed flow ratio (m_{bl}/m_0). The total pressure recovery plot known as a cane curve is a good indicator of determining how good a prediction method is. The total pressure distortion is defined by

$$\Delta p_{t2} = \frac{p_{t2,\max} - p_{t2,\min}}{\overline{p}_{t2}} . \tag{18}$$

As for the supercritical condition, the results of both turbulence models match well with the experimental data. As the state changes to the subcritical condition from the supercritical condition, the difference between the results and the experimental data widens. While the pressure recovery shows little

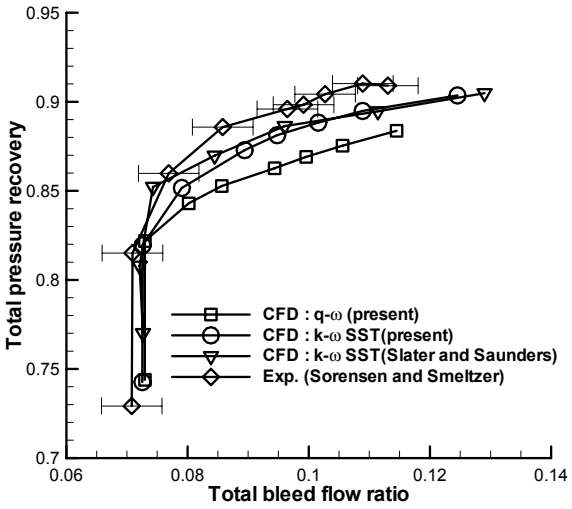

Fig. 14. Total pressure recoveries at various total bleed flow ratios.

difference from the experimental data, the bleed flow ratio shows a noticeable difference with the experimental data, especially for the $q-\omega$ model. In the subcritical condition, a terminal shock moves in the bleed regions. As a result, some parts of the bleed regions lies in the subsonic speed region. It is known that the bleed rate is sensitive to the variation of the plenum chamber pressure in the subsonic speed. The discrepancy in the subcritical condition can, therefore, result from the sensitivity of the bleed boundary condition model to the bleed plenum chamber pressure. In Fig. 13, the total pressure distortions as a function of the total bleed rate ratio are also given.

3.3.2 Case 2

As mentioned in Section 3.3, the vortex generators were placed at the subsonic diffuser for Case 2. However, the vortex generators are ignored in the simulation as done by Slater and Saunders. The vortex generators do not significantly alter the axisymmetric nature of the flow because they are located downstream of the throat and upstream of the engine face. However, the plenum chamber pressure can be different from that of the experiment if the vortex generators are ignored. Slater and Saunders adjusted the plenum chamber pressure to match the bleed rate at the supercritical condition in order to account for the difference. The plenum chamber pressure was then kept constant during the computations. Using this approach, they were able to obtain comparable results without the vortex generators because the effect of the vortex generators was limited to the downstream of vortex generators in the experiment. We adopt their approach for the computation in Case 2.

The total pressure recovery as a function of the total bleed flow ratio is presented in Fig. 14. The result of Slater and Saunders are also compared in the figure. There are noticeable differences between the results of the $q-\omega$ model and the experimental data. With the $q-\omega$ model, the total pressure recovery is predicted lower than those of the others, especially

Table 1. Total pressure recoveries and total bleed flow ratios.

	Total pressure recovery		Total bleed flow ratio	
	EXP.	CFD	EXP.	CFD
Case A	0.815	0.819	0.071	0.073
Case B	0.895	0.881	0.096	0.095
Case C	0.901	0.895	0.109	0.109

in the subcritical state. The total pressure recovery obtained with the $k-\omega$ SST model agrees well with Slater and Saunders's results, as well as with the experimental data.

Subsequent analyses are done with the $k-\omega$ SST model because this model outperforms the $q-\omega$ model. Pressure distributions on the wall are compared against experimental data at three operating conditions that were studied experimentally by Sorenson and Smeltzer. The total pressure recoveries and the bleed flow ratios at each condition are listed in Table 1. The table shows that the maximum error between the analysis results and the experimental data is about 2.8%.

The static pressure contour plots and the static wall pressure distributions along center-body and cowl are presented in Fig. 15. While Case A is at the supercritical condition, Cases B and C are both at the subcritical condition. Pressure distributions of the three cases are in good agreement with the experimental data. The effect of the vortex generators can be large at the supercritical condition as can be seen in Case A. The vortex generators are located downstream of the bleed regions and the flow there is supersonic. The vortex generators change the flow energy patterns through turbulent mixing, thus moving the terminal shock downstream in the supercritical condition. The difference in the shock location leads to the difference in the total pressure recovery. As can be seen in Fig. 15(a), the computation predicts the terminal shock further upstream, which supports this argument. For Cases B and C, the results of the computation are in good agreement with the experimental data. The flow near the vortex generators is subsonic and the effect of the vortex generators seems to be small in subcritical condition. Drastic changes in the static pressure are observed in the bleed regions. Since the bleed removes the low momentum flows inside the boundary layer, the static pressure distribution changes accordingly.

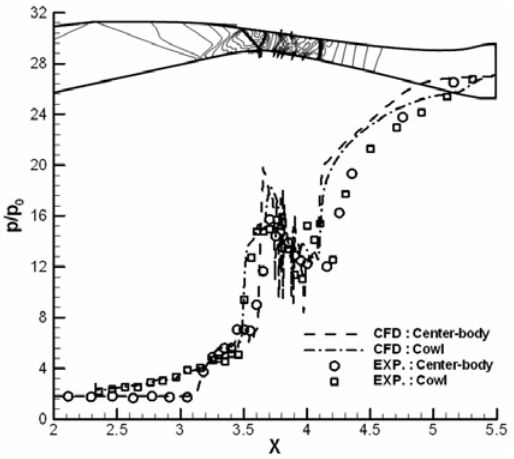

(a) Case A: supercritical condition

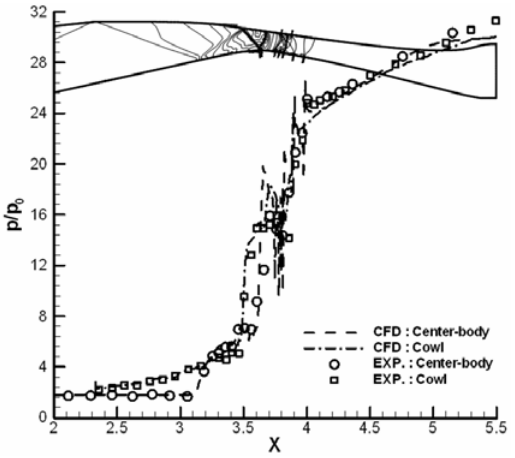

(b) Case B: subcritical condition

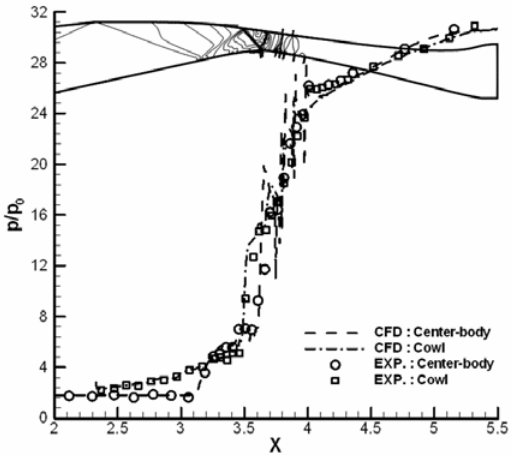

(c) Case C: subcritical condition

Fig. 15. Wall static pressure distributions and pressure contour plots at various inlet operating conditions.

4. Concluding remarks

An axisymmetric turbulence compressible solver is developed from an existing in-house code. For the simulation of flows around supersonic inlets, the bleed and the back pressure boundary conditions are incorporated into the solver. The solver is verified and validated against the experimental data for flows on a bump and over an oblique shock with bleed region. The three-step method for applying a back pressure boundary condition is proposed for the simulation of inviscid flows around a 2-D inlet. Numerical simulation of flows of the axisymmetric inlet with the multiple bleed regions is performed and the results are compared with the experimental data and other computational data. Through the simulation, the characteristics of flow around the inlet with the bleed regions are investigated. Among the turbulence models,

Menter's $k-\omega$ SST turbulence model is found to be suitable for the analysis of supersonic inlets with bleed regions. A numerical study on buzz and its control is planned in the future.

Acknowledgment

This work was supported by Inha University.

References

[1] R. D. Archer and M. Saarlas, *An introduction to aerospace propulsion*, Prentice-Hall, Inc. (1996).

[2] N. E. Sorensen and D. B. Smeltzer, Investigation of a large-scale mixed-compression axisymmetric inlet system capable of high performance at Mach numbers 06. To 3.0, NASA TM X-1507 (1968).

[3] K. W. Abrahamson, Numerical Investigation of a Mach 3.5 Axisymmetric Inlet With Multiple Bleed Zones, *AIAA paper* 88-2588 (1988).

[4] K. W. Abrahamson and D. L. Brower, An Empirical Boundary Condition for Numerical Simulation of Porous Plate Bleed Flows, *AIAA paper* 88-0306 (1988).

[5] D. W. Mayer and G. C. Paynter, Boundary condition for unsteady supersonic inlet analyses, *AIAA Journal*, 32 (6) (1994) 1200-1206.

[6] M. D. Atkinson, Numerical Investigation of A Super-Sonic Using Bleed and Micro-Ramps to Control Shock-Wave/ Boundary Layer Interactions, *AIAA paper* 2007-24 (2007).

[7] S. Lee and D. W. Choi, On Coupling the Reynolds-averaged Navier-Stokes Equations with Two-equation Turbulence Model Equations, *Int. J. Numer. Meth. Fluids*, 50 (2) (2006) 165-197.

[8] R. L. Roe, Approximate Riemann solver, parameter vectors and difference schemes, *Journal of Computational Physics*, 43 (2) (1981) 357-372.

[9] B. Van Leer, Towards the ultimate conservative difference scheme. V. A second order sequel to Godunov's method, *Journal of Computational Physics*, 32 (1) (1976) 101-136.

[10] R. M. Beam and R. F. Warming, Implicit numerical methods for the compressible Navier-Stokes and Euler equations, *von karman Institute for Fluid Dynamics Lecture Series* (1982).

[11] E. K. Kwak, Numerical simulation of supersonic inlet flow, *Master's thesis*, Inha university (2009).

[12] T. J. Coakley, Turbulence modeling Methods for the compressible Navier-Stokes equations, *AIAA paper* 83-1693 (1983).

[13] F. R. Menter, Two-equation eddy-viscosity turbulence models for engineering applications, *AIAA Journal*, 32 (8) (1994) 1598-1605.

[14] D. C. Wilcox, *Turbulence modeling for CFD,* Third Ed. DCW Industries, Inc., California, USA (2006).

[15] D. A. Johnson, C. C. Horstman and W. D. Bachalo, Comparison between experimental and prediction for a transonic turbulent separated flow, *AIAA Journal*, 20 (1982) 737-744.

[16] G. Barakos and D. Drikakis, Implicit unfactored implementation of two-equation turbulence models in compressible Navier-Stokes methods, *Int. J. Numer. Meth. Fluids*, 28 (1) (1998) 73-94.

[17] A. Eberle, 3D Euler Calculations Using Characteristic Flux Extrapolation, *AIAA paper* 85-0119 (1985).

[18] E. K. Kwak, I. Y. Yoo, D. H. Lee and S. Lee, Numerical simulations of supersonic flows using porous and rough wall boundary conditions, *Journal of computational fluids engineering*, 14 (4) (2009) 23-30.

[19] B. P. Willis, D. O. Davis and W. R. Hingst, Flowfield measurements in a normal-hole-bled oblique shock-wave and turbulent boundary-layer interaction, *AIAA paper* 95-2885 (1995).

[20] M. K. Jain and S. Mittal, Euler flow in a supersonic mixed-compression inlet, *Int. J. Numer. Meth. Fluids,* 50 (12) (2006), 1405-1423.

[21] W. E. Anderson and N. D. Wong, Experimental investigation of a large-scale, two-dimensional, mixed-compression inlet system, NASA TM X-2016 (1970).

[22] J. W. Slater and J. D. Saunders, Modeling of fixed-exit porous bleed systems, *AIAA paper* 2008-94 (2008).

Einkeun Kwak is a Ph.D. candidate of Aerodynamic Analysis and Design Laboratory at Inha University. He holds B.S. and M.S. degrees in Aerospace Engineering from Inha University. His research area includes computational fluid dynamics and its application to supersonic inlet analysis and design.

Hyungro Lee is a master student of Aerodynamic Analysis and Design Laboratory at Inha University. He received his B.S. degrees in Aerospace Engineering from Inha University in 2009. His research interests include the development of incompressible computational fluid dynamics code, and its applications.

Seungsoo Lee is a professor of Aerospace Engineering at Inha University. Prior to joining the faculty at Inha University, he was a senior research engineer at the Agency for Defense Development. He earned his Ph.D. from the Pennsylvania State University in 1990. He also holds B.S. and M.S degrees in Aeronautical and Astronautical Engineering from Seoul National University. Dr. Lee's research interests are in the area of computational fluid dynamics, overset grid method, and applied aerodynamics.